2.3.1.5.4. Comparison of Results

Examination of Figures 2.8, 2.9, and 2.10 show qualitative agreement between the LDV, PIV, and computed velocity fields, respectively, for Re = 600. Similar qualitative agreement was seen for Re = 100, 300, and 900 (Re = 2758 was not computed). However, there are quantitative differences in terms of vortex center location and velocity vector magnitude. The reason for this discrepancy is not clear.

Quantitative comparison of the LDV and PIV data is made by examining the differences between the velocity vectors measured by the two techniques. This is done by subtracting the u- and v-components of the PIV-measured velocity vectors from those measured by LDV, with the ideal difference being zero, of course. Although the channel flow above the cavity is qualitatively similar for LDV and PIV data (cf. Figs. 2.8 and 2.9), there were fairly large quantitative differences both in the channel and at the interface between the channel and the cavity. For Re = 600, the mean difference in the u_x values above the cavity was 65%. Figs. 2.8 and 2.9 show that the PIV-measured velocity was significantly lower. These differences were caused by the PIV auto-cleaning routine and the Hardy multiquadratic interpolation scheme. The auto-cleaning routine eliminates vectors based on particle pairs with a low correlation coefficient, which typically occur near walls, where there are few vectors (as mentioned above, few vectors were measured by PIV in the channel). The Hardy interpolation then uses a no-slip boundary condition at the walls which, when interpolated through the sparse near-wall velocity vectors, yields a smoothed velocity map containing lower than measured velocity vectors near the walls. Within the cavity, the agreement is better, although there is still a 10% difference in the average u_x values measured by the two techniques. The largest discrepancies are near the walls and near the cavity/channel interface. At the other Reynolds numbers, much better agreement was found between the LDV and PIV mean u-velocity values above the cavity, with differences ranging from 2.9 to 4.2%. Inside the cavity, however, the mean u-velocity difference was as high as 22% at Re = 900.

The u_y comparison in the cavity at Re = 600 indicates generally better agreement. The mean u_y in the cavity differs by 30% between the LDV and PIV data. The mean u_y above the cavity is again 65% different. Most of the discrepancy in the cavity is caused by a large difference along the upper edge of the downstream cavity wall. For the other Reynolds numbers, the agreement is better, ranging from 7.8 to 24% difference in the cavity, and from 3 to 5% above the cavity. It is not clear why the Re = 600 case has the largest differences.

The difference between the LDV and PIV data is random, not systematic, except in the channel above the cavity, where the PIV velocities were always lower for the reasons discussed above. One probable reason for the random differences between the LDV and PIV data was that they were not run simultaneously since the same laser was used for both techniques. Even if they were started at the same time, the two techniques provide different data in that the LDV data is time-averaged over the run time (typically hours for 458 points in these runs), while the PIV is quasi-instantaneous (full data set of two frames in 1/30 s). The lack of true simultaneity is important because the LDV data recorded at the beginning and end of each run showed that, even in a time-averaged sense, there

was some time variation in the flow. The main recirculating vortex center typically moved approximately 3 mm (about 9% of cavity) during the run. This can be seen by comparing LDV and PIV velocity maps (cf. Figs. 2.8 and 2.9), watching the PIV vortex center locations through several PIV sequences, or examining the LDV-measured turbulence intensity. The turbulence intensity (r.m.s. velocity fluctuations normalized by the local mean velocity) in the channel is typically one to two orders of magnitude lower than in the cavity, with the cavity peak occurring over a several millimeter region near the location of the vortex center. The source of this "unsteadiness" is unclear but is thought to be a problem in experimental conditions (e.g., room vibrations) rather than a true flow unsteadiness at these low Reynolds numbers. One possible source of the vortex movement is slight fluctuations in the head tank level (much less than 1%). Since the vortex is moving, it is difficult to compare the near-instantaneous PIV-measured velocity field with the time-averaged LDV data (averaged both over data acquisition time and between the two LDV runs). In fact, even the PIV-determined vortex centers moved on the order of 1 mm from one sequence to the next, even though these data were recorded only a few seconds to minutes apart. Since the upstream LDV-measured velocity profiles were essentially constant, the source of this vortex movement is not clear. This vortex movement is considered to be the major source of disagreement between the LDV and PIV data and the computational simulations. Figure 2.14 shows LDV and PIV measured u_x profiles through the vortex center for two of the five cases. The vortex center x location was not the same between the LDV and PIV cases, but comparing the data in this fashion eliminates the effect of vortex movement. Figure 2.14 shows good agreement within the cavity for both cases, and even in the channel above the cavity for Re = 100. The comparison for the other three Reynolds numbers showed similar good agreement within the cavity, with fairly good agreement in the channel.

The computational results show a very interesting three-dimensional structure, with the nature of the recirculating region changing at a Reynolds number of approximately 27. Unfortunately, the experiments were not well suited to examining such behavior, both because flow stability was difficult to achieve at these low Reynolds number and because the LDV and PIV experiments were run on 2D planes on the flow centerplane.

2.3.1.6. Summary and Conclusions

The shear-driven flow in a cavity was examined using two experimental techniques and computations. The flow in the cavity was driven by a fully developed laminar channel flow passing over the top of the cavity. The experimental techniques applied were laser Doppler velocimetry (LDV) and a video-based particle-tracking particle image velocimetry (PIV). The computational simulations were performed using the commercial finite element computational fluid dynamics (CFD) code FIDAP. The cavity Reynolds number ranged from 100 to 900 in the experiments, and from 0 to 1000 in the simulations.

Comparison of the experimental data indicates that the agreement between the LDV and PIV techniques is good through most of the flow but is poor near walls, especially in the channel above the cavity. This is partly due to the PIV auto-cleaning routine and the interpolation technique used

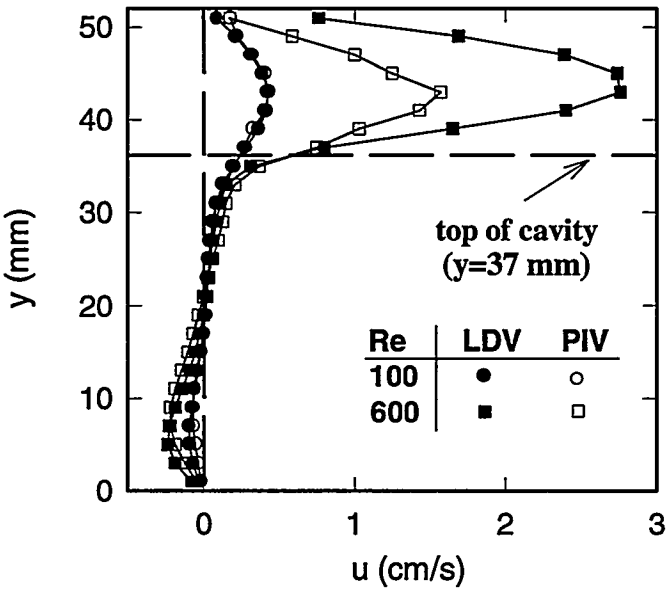

Figure 2.14. Comparison of LDV and PIV velocity profiles through the center of primary recirculation region in cavity, for Re = 100 and Re = 600.

to map the random PIV data onto a regular grid for comparison with LDV, partly due to optimization of the data acquisition for the lower speed cavity flow, and partly due to unexpected flow unsteadiness (vortex wandering). As expected, the cavity/channel flow combination was a demanding one in terms of the velocity measurement range of the PIV technique.

The computational simulations show an interesting three-dimensional structure in the recirculating region. The computed centerplane velocity map is in fair qualitative agreement with the experimental data. However, there are quantitative differences in terms of vortex center and velocity magnitude. The reasons for these discrepancies are still under investigation.

2.3.2. 2D Thermal Convection Experiments

The natural convection of a fluid in an enclosure is examined. This study is motivated by a possible magma-energy extraction system discussed by Chu et al. (1990), in which a well drilled through the Earth's crust penetrates the magma, and fluid circulation in the well keeps the rock adjacent to the penetration below the melting point (see Figure 2.15). Thus, the magma-energy extractor can be approximately described as a cold cylinder penetrating vertically downward into a hot fluid

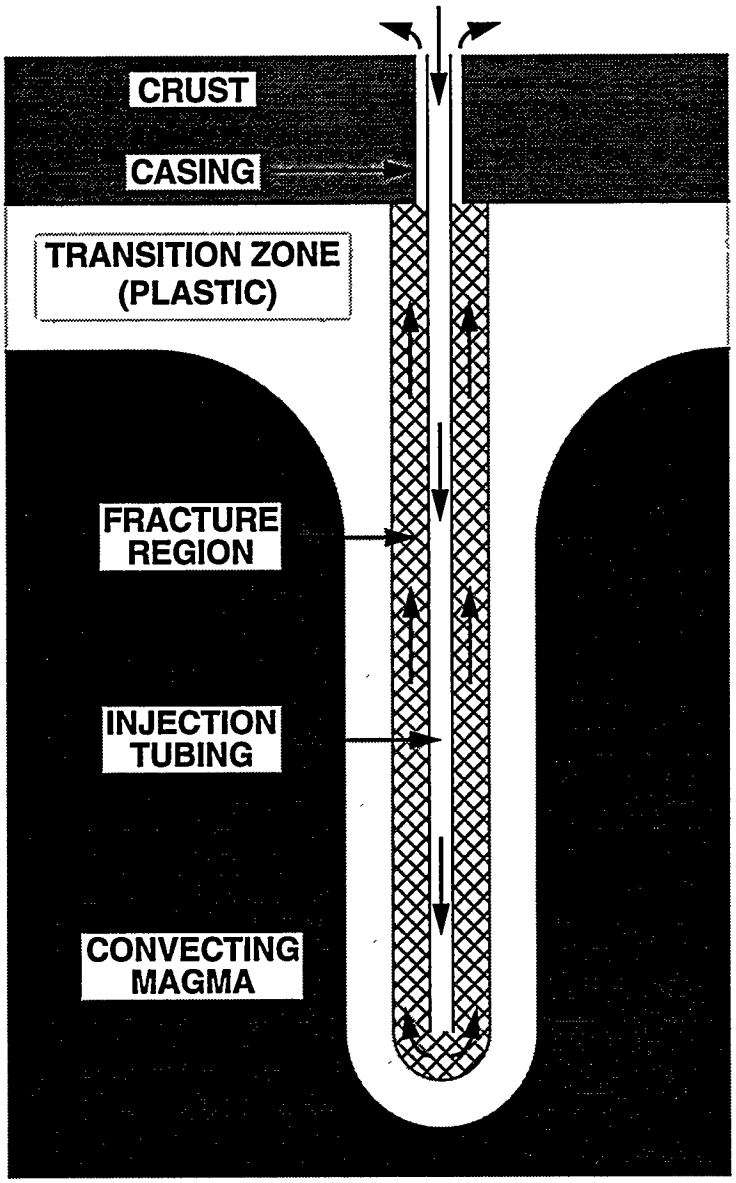

Figure 2.15. Conceptual representation of a single well of a magma-energy extraction system in operation (cf. Chu et al., 1990).

undergoing natural convection. An additional issue is that the viscosity of magma decreases strongly with increasing temperature (cf. Chu and Hickox, 1990; Hickox and Chu, 1991).

A schematic diagram of the experiment is shown in Figure 2.16. Buoyancy-driven convection is examined in a cube, where each side of the cube measures 56 cm. The bottom of the fluid-filled volume is heated with a flush mounted 14 cm by 56 cm heater, centered on the bottom surface. The top of the volume is enclosed by a water-cooled constant-temperature plate. A 28-cm long, 7.6 cm diameter cylinder, attached to the constant temperature plate, also water-cooled, protrudes into the

fluid. The vertical sides of the cube are insulated. The working fluid is 42/43 corn syrup. Because of the large viscosity variation associated with temperature, this fluid has been used in magma convection experiments (Chu and Hickox, 1990; Hickox and Chu, 1991). A three-dimensional convection flow is developed in the cubic volume as a result of the interaction between the cool downward-flowing boundary layer around the cylinder and the plume driven by the heated strip centered on the bottom surface. Because of the high viscosity of the working fluid, the flow remains laminar despite the large dimensions of the experiment, making it seem like an ideal test bed for three-dimensional PIV (see, however, Ch. 3). Glass balloons are used as tracer particles. As received, the size of the balloon ranges from 20 to 100 μm. The particles are sieved such that all particles are larger than 70 μm. Approximately 2 mg (≈0.003 cm^3) of particles are added to each 20 liter syrup container, resulting in a particle density of approximately 1 particle/cm^3. The particles stay in suspension indefinitely.

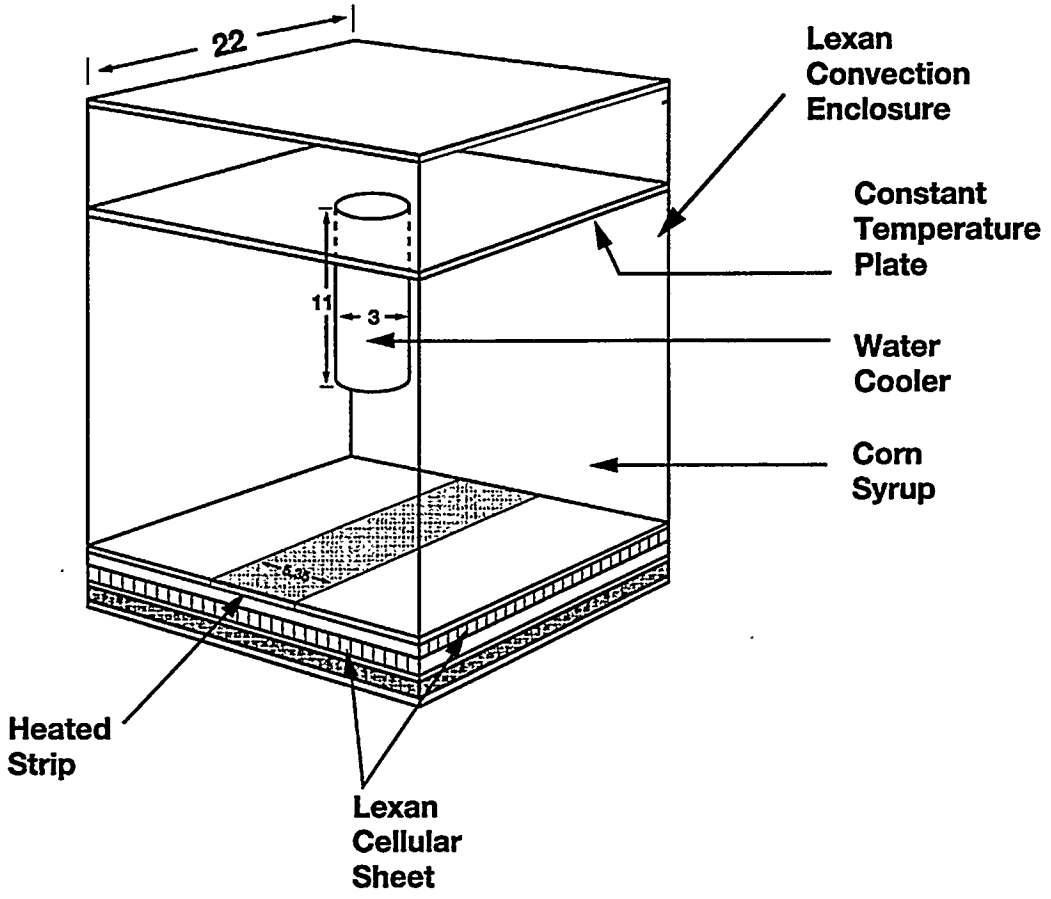

Figure 2.16. Experimental setup for thermal convection experiments. Dimensions are in inches.

The convection enclosure is an open top box with a square platform measuring 56 cm on the side and 60-cm-high and is constructed from 13-mm-thick Lexan (polycarbonate) sheets. The bottom of the box is a three-layer structure. The top layer is made of a sheet of 13-mm-thick Lexan with a

14-cm-wide center recess machined into the sheet to accept the heated strip. This top layer is glued to two 10-mm-thick Lexan glazing sheets. The glazing sheets are extruded sheets with longitudinal cells, providing structural strength and effective insulation. The heated strip consists of a 3-mm-thick copper plate with a thin, flexible, etched foil heater glued on the underside. The resistance of the foil heater is nominally 8 Ω. The temperature of the heated strip is monitored by 12 thermocouples embedded in the copper plate. In addition, there are 7 thermocouples in the unheated portion of the bottom plate. The side wall temperature is similarly monitored with 3 thermocouples. The thermocouples are made of 0.25 mm copper-constantan wires mounted flush with the surface.

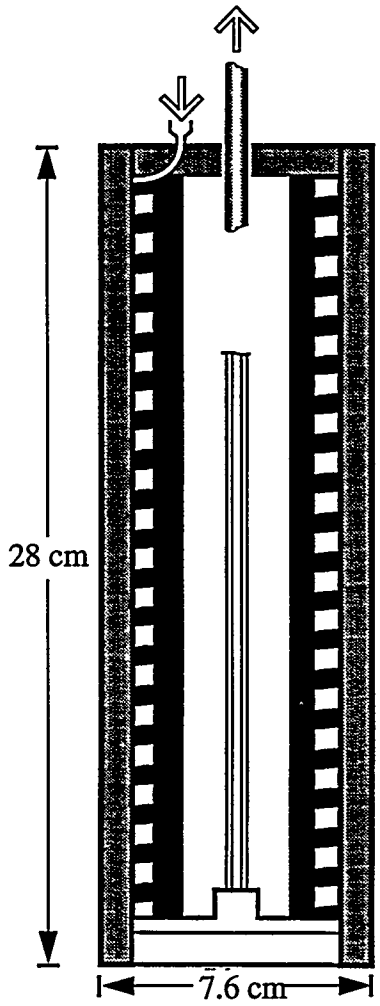

Figure 2.17. Schematic diagram of cooling cylinder inserted into convection tank.

The constant temperature plate bounding the fluid volume from above and the cylinder protruding into the fluid volume are both made of brass. The constant temperature plate is 25.4 mm thick. The temperature of the plate is maintained by the circulating cooling water, from a temperature-controlled bath (Neslab model HX-75), in twenty 13 mm by 19 mm parallel channels machined in

the back of the plate. The back of the plate is sealed by a 6-mm-thick brass plate. The cooled cylinder is a three-piece construction. The side of the cylinder is made of two pieces, one sheathed over the other (see Figure 2.17). The inner piece is essentially a 25 cm long brass screw with 13-mm by 13-mm threads on a 25.4-mm pitch. An outer piece, of 7.6-cm-diameter by 25.4-cm-long with 13 mm thick wall, slides over the inner piece to form a spiral cooling channel. The mating surfaces are slightly tapered to achieve a watertight construction. The spiral channel is connected to the bottom bulkhead consisting of concentric water channels. The plate and cylinder temperatures are monitored using Type E (Chromel-Constantan) thermocouples. During the experiment, the plate temperature was found to be uniform within 0.05°C for plate temperatures ranging from 15 to 50°C and within 0.1°C for plate temperatures below 6°C. The electric power to the heater is determined to an accuracy of 0.2%. The net rate of heat transfer to the surrounding is no more than 8% of the total electric input at steady state. The maximum total error in the determination of the Rayleigh number is 10.2%. For the two-dimensional experiments the constant-temperature plate and cylinder were kept at 20°C, and the heater was kept at 58°C.

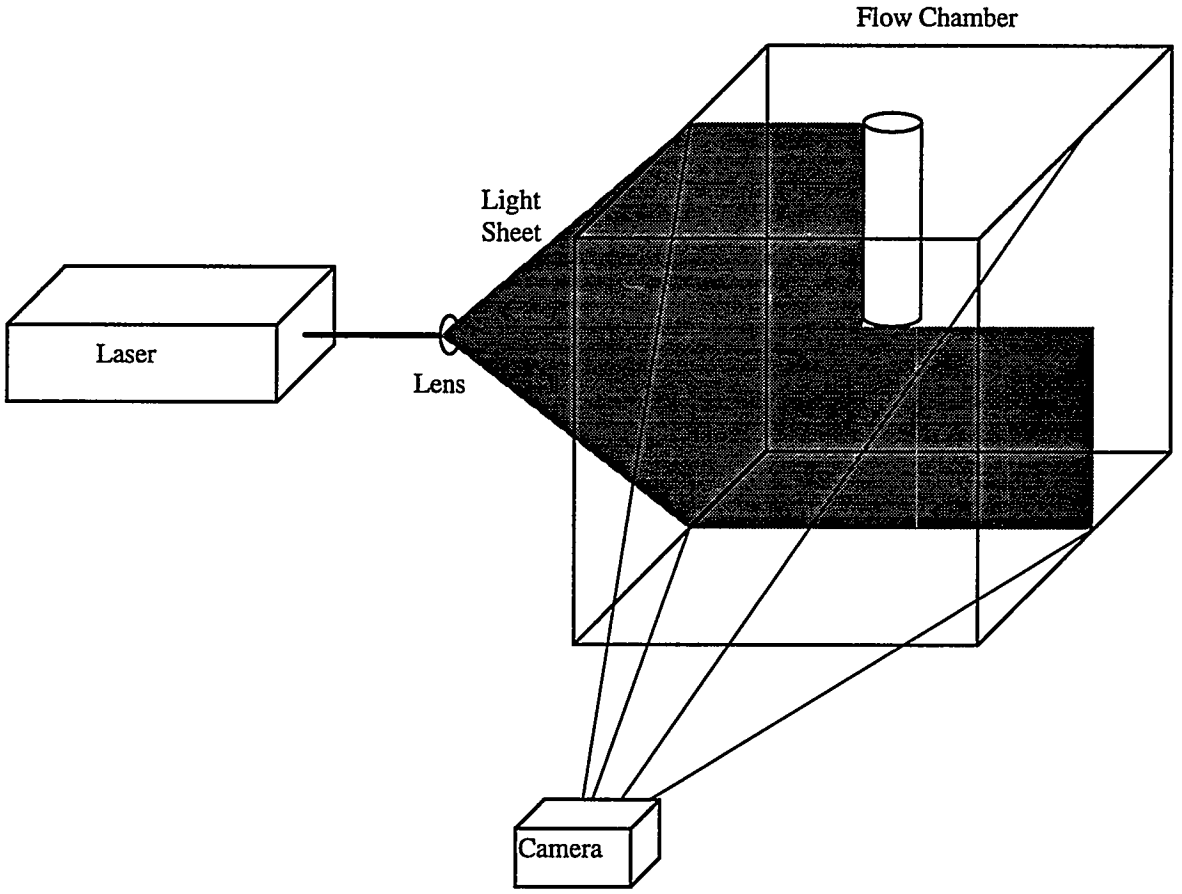

Figure 2.18. 2D PIV setup for thermal convection experiments.

Figure 2.18 shows the basic two-dimensional PIV set-up for this experiment. A light sheet was used to illuminate the particles in a plane for two-dimensional PIV. The light sheet was created by

expanding collimated laser light through a cylindrical lens. A Spectra-Physics model 165 Argon ion laser was used to produce the light. Pictures of the illuminated particles were captured using a 35 mm film camera. These pictures were digitized using a Nikon Coolscan on a 486-based computer.

2.3.2.1. Results

The two-dimensional PIV routines worked fairly well for this experiment. Figures 2.19 shows flow-visualization photographs for the center planes intersecting and bisecting the heater strip. Figures 2.20 are PIV results for equivalent planes.

Figure 2.21 shows finite element CFD simulation of selected streamlines in the symmetry planes. Details of the computational techniques are given in Chapter 3. Figures 2.22 shows streamlines calculated from the PIV velocity fields given in Figures 2.20. Qualitative agreement of the streamlines between experiment and computation can be seen.

Unfortunately, the computational models were unable to converge at the high temperatures used in the experiment, so an exact comparison was impossible. However, the flow computed at lower temperatures is very similar to the flow shown by the PIV results at higher temperature.

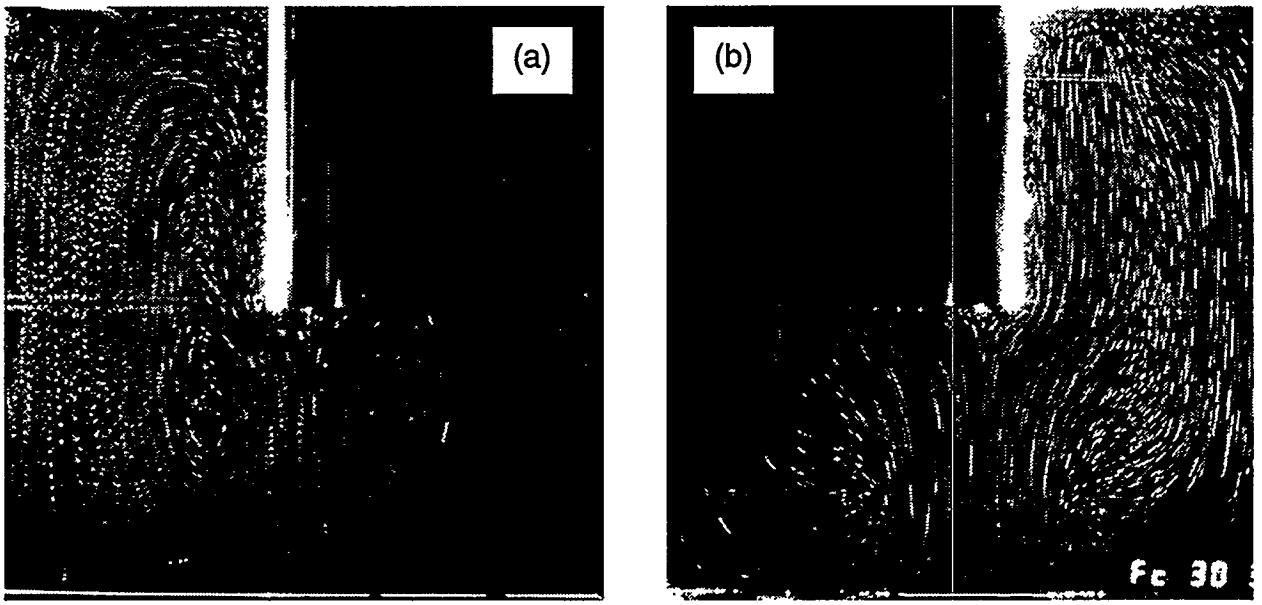

Figure 2.19. Laser light sheet flow-visualization photographs: (a) slice through cylinder along heater, (b) slice through cylinder across heater.

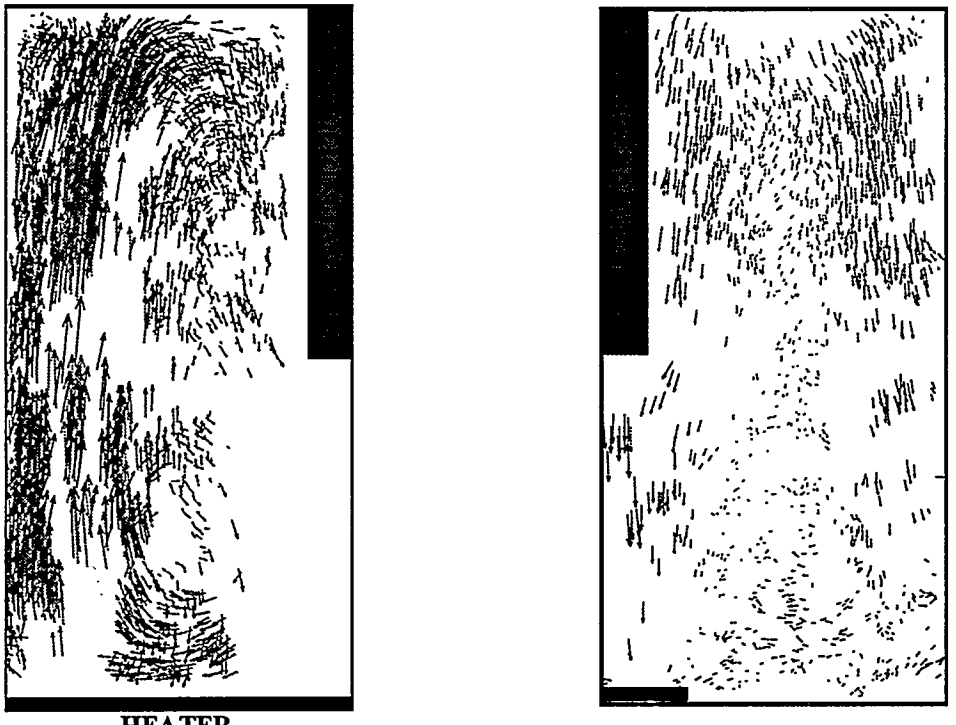

Figure 2.20. PIV velocity vectors at similar conditions. Left, slice through cylinder along heater strip (plane x = 0); right, slice through cylinder across heater plane (plane y = 0). The flow pattern agrees with the flow visualization. Flow is downward beneath cylinder.

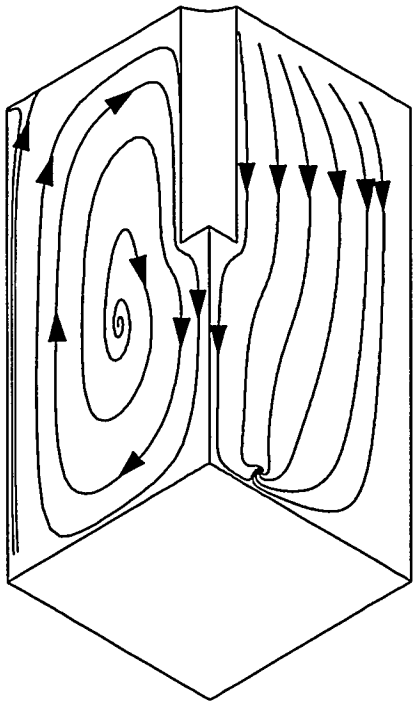

Figure 2.21. Finite element CFD simulation of selected streamlines in the symmetry planes.

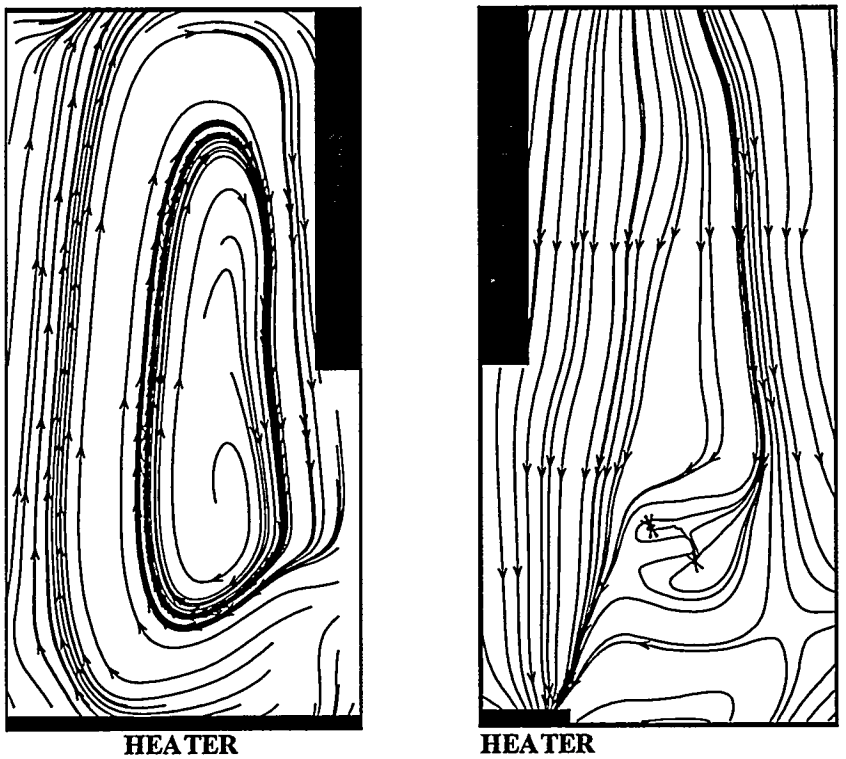

Figure 2.22. Streamlines calculated from PIV velocity fields given in Figure 2.20. Qualitative agreement with the computational simulation in Figure 2.21 can be seen.

3. THREE-DIMENSIONAL PARTICLE IMAGE VELOCIMETRY

3.1 Introduction

The measurement of 3D velocity vectors in 3D flows requires measurement of all three velocity components (u_x, u_y, and u_z in the x, y, and z directions, respectively). Traditional 3D velocity measurement techniques include LDV and hot wire anemometry. Both of these techniques require complicated experimental configurations and expensive data acquisition and processing electronics, and make measurements at only a specific point in the flow field. To measure the full flow field requires traversing the point measurement region, effectively limiting applicability to steady flows.

Standard two-dimensional PIV provides a detailed planar velocity map, well suited to 2D flow fields, but cannot measure the out-of-plane velocity component of a 3D flow. In fact, errors arise in 2D PIV when out-of-plane motion becomes appreciable. Obviously, particles entering or leaving the illuminated plane during the image data acquisition period will weaken the correlation and lead to the possibility of false vector identification.

A techniques for 3D PIV will be investigated here, based on volume illumination of the flow field, recording particle motion with multiple cameras.

3.2 Three-Dimensional PIV

The method of 3D PIV chosen here is stereo views taken of the flow using multiple cameras (see Figure 3.1). This technique has been applied by other researchers, but according to Grant (1994), the use of stereo views "presents problems in image matching that have a timeless appeal and provide potential for future work." In addition, Grant states that "accurate calibration of the relationship between object and images is still the subject of discussion." The results of this investigation support these statements.

3.2.1. Camera Calibration and Particle Combination Theory

Before tracking the particles through three dimensions, it is necessary to combine the separate camera image frames into a three-dimensional space frame. Since it is not obvious which particle is which in the separate image frames, this step can introduce error into the analysis of the data. Therefore, three cameras are normally used to minimize the error in locating the seeds. Linearized equations relate the location of a particle in a two-dimensional image axis to its three-dimensional world position (Gonzalez and Wintz, 1987). In order to use these equations, however, the precise location and orientation of the camera must be determined. These can be found by measuring the exact position and rotation of the camera and adjusting them for refraction, or they can be

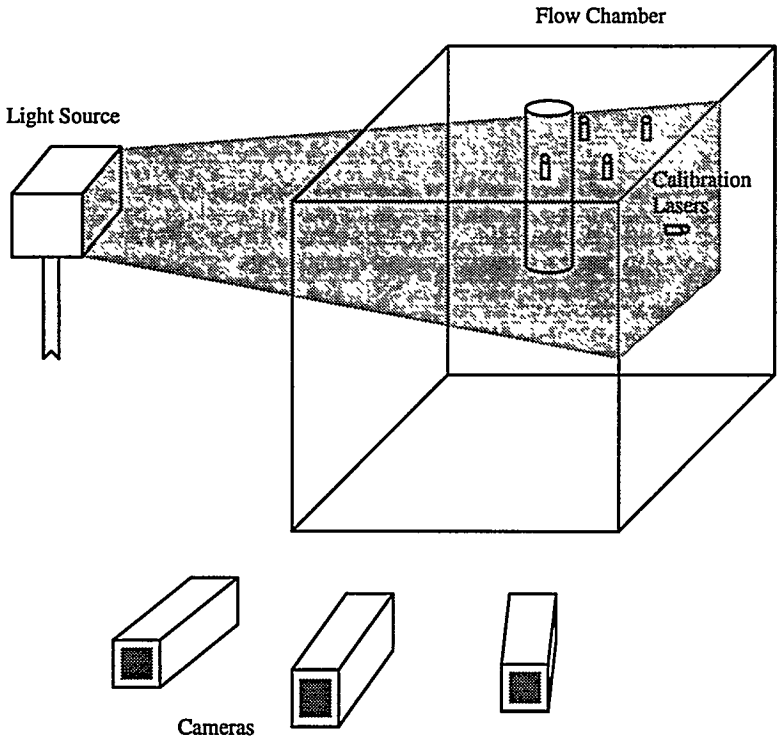

Figure 3.1 Three-Dimensional PIV set-up.

calculated by recording an image of known world positions. The method for calculating the variables from known world and camera positions is detailed here.

The equations relating a position in the world to a position in the camera are nonlinear. This is because of the perspective change through the focal point. However, by using a linear transformation, the process of relating the camera to the world is greatly simplified. Equation 1 displays the coordinates of a world point, W. This point is transformed into a homogenous world

point, W_h, (Eq. 2), by the introduction of a new dimension k_w. To return to a normal world point, the first three indices of the homogenous world vector are simply divided by the fourth index.

$$W = \begin{bmatrix} X_w \\ Y_w \\ Z_w \end{bmatrix} \tag{1}$$

$$W_h = \begin{bmatrix} k_w X_w \\ k_w Y_w \\ k_w Z_w \\ k_w \end{bmatrix} \tag{2}$$

By using W_h, the homogenous camera point, C_h, can be obtained simply by multiplying W_h by the perspective transformation matrix, P, given by Eq. 3.

$$P = \begin{bmatrix} 1 & 0 & 0 & 0 \\ 0 & 1 & 0 & 0 \\ 0 & 0 & 1 & 0 \\ 0 & 0 & -1/\lambda & 1 \end{bmatrix} . \tag{3}$$

The perspective change is caused by all the light passing through the focal point of the camera before intersecting the camera XY axes. This focal point is separated from the camera origin by the focal length, λ, which is perpendicular to camera XY axes and is measured in camera units. This only works if the world axes and camera axes are perfectly aligned. Since this is too restrictive, especially with multiple cameras, it is necessary to use other transformations to first scale, translate, and rotate the world axes to match the camera axes. This is done with the scaling transformation matrix, S, the rotation transformation matrix, R, and the translation transformation matrix, T, shown in Equations 4, 5, and 6. These are then combined with P into the complete transformation matrix, A, as shown in Eq. 7. The scaling factors S_x, S_y, and S_z multiply the world axes to obtain the camera axes, and are measured in camera units/world units. The angles α, β, and

measure the rotation around the x, y, and z axes respectively needed to match up the camera and world axes. The distances Δx, Δy, and Δz measure the distance between the world and camera origins in world units.

$$S = \begin{bmatrix} S_x & 0 & 0 & 0 \\ 0 & S_y & 0 & 0 \\ 0 & 0 & S_z & 0 \\ 0 & 0 & 0 & 1 \end{bmatrix} \tag{4}$$

$$R = R_\beta R_\alpha R_\theta = \begin{bmatrix} \cos\beta & 0 & -\sin\beta & 0 \\ 0 & 1 & 0 & 0 \\ \sin\beta & 0 & \cos\beta & 0 \\ 0 & 0 & 0 & 1 \end{bmatrix} \begin{bmatrix} 1 & 0 & 0 & 0 \\ 0 & \cos\alpha & \sin\alpha & 0 \\ 0 & -\sin\alpha & \cos\alpha & 0 \\ 0 & 0 & 0 & 1 \end{bmatrix} \begin{bmatrix} \cos\theta & \sin\theta & 0 & 0 \\ -\sin\theta & \cos\theta & 0 & 0 \\ 0 & 0 & 1 & 0 \\ 0 & 0 & 0 & 1 \end{bmatrix} \tag{5}$$

$$T = \begin{bmatrix} 1 & 0 & 0 & \Delta x \\ 0 & 1 & 0 & \Delta y \\ 0 & 0 & 1 & \Delta z \\ 0 & 0 & 0 & 1 \end{bmatrix} \tag{6}$$

$$A = PSRT \tag{7}$$

Using A, it is possible to transform any world point into a camera point for a camera located anywhere. C_h is obtained simply by multiplying W_h by A, as shown in Eq. 8. The camera point, C, is then obtained by dividing the first three indices of C_h by the fourth index, as shown in Eq. 9.

$$C_h = \begin{bmatrix} k_c X_c \\ k_c Y_c \\ k_c Z_c \\ k_c \end{bmatrix} = AW_h = \begin{bmatrix} k_w (a_{11}X_w + a_{12}Y_w + a_{13}Z_w + a_{14}) \\ k_w (a_{21}X_w + a_{22}Y_w + a_{23}Z_w + a_{24}) \\ k_w (a_{31}X_w + a_{32}Y_w + a_{33}Z_w + a_{34}) \\ k_w (a_{41}X_w + a_{42}Y_w + a_{43}Z_w + a_{44}) \end{bmatrix} \tag{8}$$

$$C = \begin{bmatrix} X_c \\ Y_c \\ Z_c \end{bmatrix} = \begin{bmatrix} (a_{11}X_w + a_{12}Y_w + a_{13}Z_w + a_{14}) / (a_{41}X_w + a_{42}Y_w + a_{43}Z_w + a_{44}) \\ (a_{21}X_w + a_{22}Y_w + a_{23}Z_w + a_{24}) / (a_{41}X_w + a_{42}Y_w + a_{43}Z_w + a_{44}) \\ (a_{31}X_w + a_{32}Y_w + a_{33}Z_w + a_{34}) / (a_{41}X_w + a_{42}Y_w + a_{43}Z_w + a_{44}) \end{bmatrix} \tag{9}$$

Thus it is possible to transform a known world point into a camera point for a camera with known focal length, scaling, rotation, and location. This is useful for creating synthetic data, but not much else. However, we can rearrange the equations in order to locate the cameras, and then use that information to do the reverse transformation. By rearranging the equations for X_c and Y_c, Equations 10 and 11 can be obtained.

$$(a_{11}X_w + a_{12}Y_w + a_{13}Z_w + a_{14}) - X_c(a_{41}X_w + a_{42}Y_w + a_{43}Z_w + a_{44}) = 0 \quad (10)$$

$$(a_{21}X_w + a_{22}Y_w + a_{23}Z_w + a_{24}) - Y_c(a_{41}X_w + a_{42}Y_w + a_{43}Z_w + a_{44}) = 0 \quad (11)$$

Using these two equations with known camera and world points, it is possible to solve for the coefficients of the transformation matrix, A. With six known world points and their corresponding camera points, the twelve coefficients used can be solved for. However, since the equations are homogeneous, it is necessary to fix one of the coefficients, with the other eleven being proportional to it. Once these coefficients are found, the various variables that make them up can be solved for using non-linear equations. These variables are the focal length, scaling, rotation, and location of the camera.

Once the variables that make up the coefficients of the transformation matrix are found, then all sixteen coefficients can be solved for, and the inverse process can be found. The inverse process is simply A^{-1}, and it can be used for solving for the homogenous world points as shown in Equations 12 and 13.

$$A^{-1} = T^{-1}R^{-1}S^{-1}P^{-1} \quad (12)$$

$$W_h = A^{-1}C_h \quad (13)$$

However, when the inverse process is solved it requires Z_c, which cannot be measured using one camera. So, instead of using the direct inverse process, a slightly different process is used. The location of a homogenous camera point is found on the world axes using Eq. 14. Similarly, the location of the focal point can be found in world coordinates as shown in Eq. 15. Neither of these equations uses the perspective transformation, since the actual position of these points is desired.

The non-homogeneous position can be solved for simply by dividing by the fourth index, as before. Thus the actual position of the camera point and the focal point is obtained on the world axes.

$$W_{ch} = \begin{bmatrix} k_w X_{wc} \\ k_w Y_{wc} \\ k_w Z_{wc} \\ k_w \end{bmatrix} = T^{-1}R^{-1}S^{-1} \begin{bmatrix} k_c X_c \\ k_c Y_c \\ 0 \\ k_c \end{bmatrix} \tag{14}$$

$$W_{fh} = \begin{bmatrix} k_w X_{wf} \\ k_w Y_{wf} \\ k_w Z_{wf} \\ k_w \end{bmatrix} = T^{-1}R^{-1}S^{-1} \begin{bmatrix} 0 \\ 0 \\ k_c \lambda \\ k_c \end{bmatrix} \tag{15}$$

Using these points, a line can be drawn on the world axes, as shown in Eq. (16). The world point that corresponds to the camera point used to make this line must be somewhere along this line. A similar line can be drawn from a corresponding point in a second camera. Where these two lines intersect the original world point is located. This is demonstrated in two dimensions by Fig. 3.2.

$$L_h = \begin{bmatrix} X_L \\ Y_L \\ Z_L \end{bmatrix} = \begin{bmatrix} X_{wf} \\ Y_{wf} \\ Z_{wf} \end{bmatrix} + j \begin{bmatrix} X_{wc} \\ Y_{wc} \\ Z_{wc} \end{bmatrix} \tag{16}$$

The process is more complicated in three dimensions. In three dimensions, the lines should still theoretically cross, but with the introduction of error they no longer cross. So instead of finding the intersection of the two lines, differentiation is used to find where the lines are closest to each other. The world point is then located centered between the two lines. Another problem arises from the fact that the correspondence of points in one camera to points in the other camera is unknown. Thus, every point in the second camera must be used to draw a line to find the best match for each point in the first camera. The point in the second camera whose line comes closest to the line created by the point in the first camera is assumed to be the corresponding point. With only two cameras, it is impossible to discriminate wrong matches from correct matches, so a third camera is used to check. If all three cameras agree on the point, then it is used. If not, then the point is dropped. By this method, any point produced by the process should be approximately in the correct position.